Tago Tetsuro (Orcid ID: 0000-0002-9545-0922)

Radiosynthesis and preliminary evaluation of an ^{18}F-labeled Tubastatin A analogue for PET imaging of histone deacetylase 6

Tetsuro Tago, Jun Toyohara, Kenji Ishii

Research Team for Neuroimaging, Tokyo Metropolitan Institute of Gerontology, 35-2 Sakae-cho, Itabashi-ku, Tokyo 173-0015, Japan.

Corresponding author: Jun Toyohara, Ph.D.

Research Team for Neuroimaging, Tokyo Metropolitan Institute of Gerontology, 35-2 Sakae-cho, Itabashi-ku, Tokyo 173-0015, Japan

Tel: +81-3-3964-3241; Fax: +81-3-3964-1148

toyohara@pet.tmig.or.jp

Short title: Fluorine-18-labeled HDAC6 ligand

This article has been accepted for publication and undergone full peer review but has not been through the copyediting, typesetting, pagination and proofreading process which may lead to differences between this version and the Version of Record. Please cite this article as doi: 10.1002/jlcr.3823

This article is protected by copyright. All rights reserved.

Abstract (199/200 words)

Histone deacetylase 6 (HDAC6) is a unique member of the HDAC family because of its characteristics, namely its cytoplasmic localization and ubiquitin binding. HDAC6 has been implicated in cancer metastasis and neurodegeneration. In the present study, we performed radiosynthesis and biological evaluation of a fluorine-18-labeled ligand [^{18}F]**3**, which is an analogue of the HDAC6-selective inhibitor Tubastatin A, for PET imaging. [^{18}F]**3** was synthesized by a two-step reaction composed of ^{18}F-fluorination and formation of a hydroxamic acid group. IC_{50} values of **3** against HDAC1 and HDAC6 activities were 996 and 33.1 nM, respectively. A biodistribution study in mice demonstrated low brain uptake of [^{18}F]**3**. Furthermore, bone radioactivity was stable at around 2% ID/g after injection, suggesting high tolerance to defluorination. Regarding metabolic stability, 70% of the compound was observed as the unchanged form at 30 min post injection in mouse plasma. A small animal PET study in mice showed that pre-treatment with cyclosporine A had no effect on initial brain uptake of [^{18}F]**3**, suggesting low brain uptake of [^{18}F]**3** was not caused by the P-glycoprotein-mediated efflux. While PET imaging using [^{18}F]**3** has a limitation with respect to neurodegenerative diseases, further studies evaluating its utility for certain cancers are worth evaluating.

Keywords: Histone deacetylase 6, Positron emission tomography, Tubastatin A, Fluorine-18

This article is protected by copyright. All rights reserved.

1. INTRODUCTION

Histone deacetylases (HDACs) are enzymes that catalyze the deacetylation of acetylated lysine residues of histones, which are the major components of chromatin.[1] The HDAC family has been classified into five classes according to their homology to yeast HDACs: class I (HDAC1, 2, 3, and 8), class IIa (HDAC4, 5, 7, and 9), class IIb (HDAC6 and 10), class III (sirtuins (SIRT1–7)), and class IV (HDAC11).[2-4] Except for sirtuins, which have nicotinamide adenine dinucleotide-dependent catalytic activity, HDACs have a zinc dependent catalytic site.[5] Acetylation of lysine residues in the N-termini of histones neutralizes their positive charge, which weakens the interaction between histones and negatively charged DNA, thereby allowing enhanced accessibility of transcription factors to the DNA.[6] Abnormalities in such epigenetic regulatory system are important factors in the development of diseases including cancer and neurodegeneration; therefore, HDACs are considered promising therapeutic targets for these diseases.[7-11] For instance, suberoylanilide hydroxamic acid (SAHA, also known as vorinostat) is a non-selective HDAC inhibitor that is the first US Food and Drug Administration-approved hydroxamic acid-based drug for use in patients with cutaneous T-cell lymphoma.[3]

HDAC6, which belongs to the class IIb, is a unique member because of its characteristic localization and functions. HDAC6 has two nuclear exclusion domains and one cytoplasmic anchoring domain, rendering it primarily localized in the cytoplasm.[12] HDAC6 also has two

This article is protected by copyright. All rights reserved.

Accepted Article

catalytic domains with different substrate specificities,[13] and catalyzes the deacetylation of non-histone proteins such as α-tubulin, HSP90, cortactin, and the microtubule-associated protein tau.[14,15] Deacetylation of α-tubulin in microtubules increases cell motility and enhances cancer cell metastasis and invasion.[16,17] Additionally, HDAC6 has an ubiquitin binding domain and is involved in the degradation of misfolded and ubiquitinated proteins.[18,19] HDAC6 also has a binding domain against the cytoskeletal motor protein dynein and couples ubiquitinated proteins to dynein motors, thereby mediating their transport along microtubules to aggresomes.[20,21] These characteristics of HDAC6 have spurred interest in targeting it with therapeutics for cancers and neurodegenerative diseases,[14,22] with several clinical trials of selective HDAC6 inhibitors for cancers having been performed.[23]

In the past decade, a number of radiolabeled HDAC ligands for positron emission tomography (PET) imaging have been developed.[24-26] Besides the detection of regions with abnormalities in HDAC expression levels, PET imaging can contribute to the development of HDAC inhibitor drugs by enabling the assessment of target engagement.[27,28] The majority of HDAC radioligands, including the first SAHA-based HDAC radioligand [^{18}F]FAHA, are hydroxamic acid-based with others being benzamide-based or carboxylic acid-based.[24,29] In most cases, HDAC radioligands show poor blood-brain barrier (BBB) permeability in rodents and non-human primates, probably due to the high-polarity of the hydroxamic acid group.[24] However, Hooker et al. reported that hydroxamic acid-based radioligands containing an adamantane

This article is protected by copyright. All rights reserved.

Accepted Article

group, which is often conjugated with drugs to improve their brain penetrance,[30,31] readily crossed the BBB in rodents and non-human primates.[32,33] In particular, the carbon-11 labeled ligand [^{11}C]Martinostat which has high binding affinity for class I HDACs underwent a first-in-human study to evaluate neuroepigenetic regulation.[34] As expected, [^{11}C]Martinostat demonstrated excellent uptake in the human brain, and higher uptake was observed in the cortical gray matter compared with white matter. Furthermore, [^{11}C]Martinostat PET was also used to image HDAC dysregulation in patients with schizophrenia.[35]

Due to the characteristics of HDAC6, selective imaging of HDAC6 could facilitate research into its roles in cancers and neurodegenerative diseases. Regarding the development of HDAC6 selective radioligands, Lu et al. reported on ^{11}C-carbonylation methods for labeling Tubastatin A, an HDAC6 selective inhibitor (**1** in Figure 1),[36] that employed [^{11}C]carbon monoxide.[37] Radiosynthesis of the Tubastatin A analogue [^{11}C]KB631 ([^{11}C]**2** in Figure 1) with [^{11}C]methyl iodide was also reported by Lu et al.,[38] and its preclinical evaluation for visualization of B16F10 melanoma has recently been reported by Vermeulen et al.[39] Additionally, [^{18}F]Bavarostat was developed by Strebl et al.[40] as an adamantane-conjugated HDAC6 selective radioligand. Although [^{18}F]Bavarostat needs a unique ruthenium-mediated ^{18}F-deoxyfluorination[41] for its radiosynthesis, its BBB permeability and specific binding in the brain was confirmed by in vivo blocking studies in non-human primates.

Here, we report the development of a novel ^{18}F-labeled Tubastatin A analogue [^{18}F]**3** (Figure

This article is protected by copyright. All rights reserved.

1) as an HDAC6 selective PET imaging ligand. We expected that the basic structure of Tubastatin A analogues was acceptable for structural modification for labeling with fluorine-18, which has a relatively long half-life (109 min) that allows centralized production of radiopharmaceuticals, because the relationship between the structures of the analogues and their HDAC6 selectivity were well known.[36,42] The chemical structure of **1** consists of three motifs: a hydroxamic acid zinc-binding group that localizes a zinc ion within the HDAC active site, a carboline-based cap group that interacts with the protein surface of the binding pocket, and a benzyl linker group that bridges the two groups. The benzyl linker and carboline cap groups contribute to the selectivity for HDAC6, which has a wider and shallower catalytic channel compared with that of HDAC1. Kalin et al. demonstrated that a substituent could be introduced at the nitrogen atom of tetrahydropyridine of the β-carboline regioisomer of **1** without seriously disrupting HDAC6 selectivity.[42] Therefore, we decided to substitute the methyl group of **2** with a fluoroethyl group for ^{18}F-labeling of the Tubastatin A analogue. Radiosynthesis of [^{18}F]**3** was achieved using a two-step reaction composed of ^{18}F-fluorination by general nucleophilic substitution and conversion of a methylester group into a hydroxamic acid group. We intended to perform this radiosynthesis without intermediary solid-phase extraction or high-performance liquid chromatography (HPLC) purification steps, which have been incorporated in other hydroxamic acid-based radioligands,[32,40,43] because these processes often complicate automated radiosynthesis. In addition, preclinical evaluations such as binding

This article is protected by copyright. All rights reserved.

selectivity assays and biodistribution assays were performed to assess the potential utility of [^{18}F]**3** for visualization of HDAC6.

Accepted Article

This article is protected by copyright. All rights reserved.

2. EXPERIMENTAL

2.1. General

An aqueous solution of tetrabutylammonium hydrogen carbonate (0.075 M) was purchased from ABX GmbH (Radeberg, Germany). Other reagents were purchased from Sigma-Aldrich (St. Louis, MO), Tokyo Chemical Industry (Tokyo, Japan), or FUJIFILM Wako Pure Chemical (Osaka, Japan). Automated flash chromatography was performed using an EPCLC AI-580 (Yamazen Science, Osaka, Japan). ^{1}H-Nuclear magnetic resonance (NMR) spectra were recorded on a JEOL Model ECP-400 (400 MHz; JEOL, Tokyo, Japan) or a Bruker AVANCE III HD 400 (400 MHz; Bruker, Billerica, MA). Chemical shifts (δ) are relative to TMS (0 ppm) and coupling constants are expressed in Hertz (Hz). Multiplicity was defined as following abbreviations: s = singlet, d = doublet, t = triplet, dd = double doublet, m = multiplet, br = broad. Electrospray ionization-mass spectrometry (ESI-MS) was measured using an LCT Premier XE (Waters, Milford, MA). High-resolution mass spectrometry (HRMS) (ESI) was carried out with a Q Exactive equipped with an UltiMate 3000 HPLC system (Thermo Fisher Scientific, Waltham, MA).

2.2. Chemistry

Methods for the synthesis and characterization of non-radioactive **2**, compounds shown in Scheme 1, and the precursor of [^{11}C]**2** are described in detail in the Supporting Information.

This article is protected by copyright. All rights reserved.

Accepted Article

2.3. Radiosynthesis

A method for the radiosynthesis of [^{11}C]**2** is described in the Supporting Information.

Automated radiosynthesis, purification, and formulation of the [^{18}F]**3** injection solution were performed using a modified F100 synthesizer (Sumitomo Heavy Industries, Tokyo, Japan). [^{18}F]Fluoride was produced by proton irradiation of ^{18}O-enriched water (Taiyo Nippon Sanso, Tokyo, Japan) at 50 μA for 15 min using an HM-20 cyclotron (Sumitomo Heavy Industries). The irradiated ^{18}O-enriched water containing [^{18}F]fluoride was passed through a Sep-Pak Accell Plus QMA Plus Light cartridge (Waters), and the trapped [^{18}F]fluoride was eluted with a mixture of 0.075 M tetrabutylammonium hydrogen carbonate (0.5 mL) and acetonitrile (0.5 mL) to a reaction vessel. After the solvent was dried azeotropically, 1 mL of dry acetonitrile was added, and azeotropic drying was repeated. A mixture of precursor (**8**) in acetonitrile (2 mg/700 μL) was added to the reaction vessel, and the reaction mixture was heated at 90 °C for 15 min. After removal of the reaction solvent by heating at 90 °C under a slow helium stream, the reaction vessel was cooled to 30 °C. A mixture of 50% hydroxylamine aqueous solution (0.1 mL) and 2 M sodium hydroxide in methanol (0.2 mL) was added to the residue and stirred at the same temperature for 10 min. Thereafter, 0.5 M hydrogen chloride (1.2 mL) was added and the reaction mixture was purified by semi-preparative HPLC equipped with a radioactivity detector system [Column: YMC-Pack Pro C18 RS, 5 μm, 10×250 mm (YMC, Kyoto, Japan);

This article is protected by copyright. All rights reserved.

Eluent: acetonitrile/25 mM ammonium formate (adjusted to pH 4.7 with formic acid) = 30/70; Flow rate: 4.5 mL/min; UV: 260 nm]. The fraction containing the product was combined with 250 mg/mL ascorbic acid injection solution (0.2 mL) and the solvent was removed by evaporation. Finally, the residue was formulated in physiological saline and the product was analyzed with an analytical HPLC [Column: Sunniest C18, 5 μm, 4.6×150 mm (ChromaNik Technologies, Osaka, Japan); Eluent: acetonitrile/water/trifluoroacetic acid in water = 27.5/72.5/0.1; Flow rate: 1.0 mL/min; UV: 254 nm]. Representative semi-preparative HPLC and analytical HPLC chromatograms are shown in the Supporting Information.

2.4. Log *D* determination

A saline solution containing [^{18}F]**3** (300 kBq) was added to a centrifuge tube containing 3 mL of 1-octanol and 3 mL of Dulbecco's phosphate-buffered saline. The centrifuge tube was vortexed for 20 sec and rested for 10 sec; this procedure was repeated twice. The 1-octanol and aqueous phases were separated by centrifugation (720×*g* for 3 min at rt). An aliquot of the 1-octanol phase (2 mL) was transferred into a centrifuge tube containing 1 mL of 1-octanol and 3 mL of Dulbecco's phosphate-buffered saline, and the previous mixing and centrifugation procedures were repeated. These processes, from the transfer of the 1-octanol phase to centrifugation, were repeated once more. Aliquots (100 μL) were collected from both the 1-octanol and aqueous phases, and the radioactivity of each sample was measured with a gamma

This article is protected by copyright. All rights reserved.

Accepted Article

counter (2480 Wizard^2; PerkinElmer, Waltham, MA). The log *D* value was determined using the following equation: log *D* = log(radioactivity of 1-octanol sample/radioactivity of aqueous sample).

2.5. In vitro HDAC enzyme inhibition assay

Binding affinities of **2** and **3** for HDAC1 and HDAC6 were measured using HDAC1 and HDAC6 Fluorogenic Assay Kits (BPS Bioscience, San Diego, CA), respectively, following the protocol described in the product datasheet. IC_{50} values were determined from dose-response curves using GraphPad Prism software (GraphPad Software, San Diego, CA).

2.6. Ex vivo biodistribution assay in normal mice

All experiments using mice were approved by the Animal Experiment Committee of Tokyo Metropolitan Institute of Gerontology and carried out in accordance with its animal experimental protocols (Authorization number: 17081 and 18013). A saline solution containing [^{11}C]**2** (4.8 MBq/200 μL) or [^{18}F]**3** (0.77 MBq/200 μL) was administered to ddY mice (8 week-old, male, 33.1 ± 1.8 g; Japan SLC, Hamamatsu, Japan; n = 4 per time point) via the tail vein. The mice were killed by decapitation at 1, 5, 10, 30, and 60 min post-injection, and the organs of interest were collected. After the samples were weighed, the radioactivity was counted with a gamma counter (1282 CompuGamma CS, LKB Wallac, Turku, Finland).

This article is protected by copyright. All rights reserved.

Accepted Article

2.7. Metabolite analysis of [^{18}F]3 in mice

A saline solution of [^{18}F]**3** (37 MBq) was injected to ddY mice (8 week-old, male; Japan SLC; n = 3 per time point) via the tail vein. The mice were killed by decapitation at 15 and 30 min post-injection, and cardiac blood was collected using a heparinized syringe and kept on ice. Plasma fractions were separated from the blood by centrifugation (7,000×*g* for 1 min at 4 °C). The plasma (200 μL) was deproteinized by addition of a 2-equivalent volume (400 μL) of acetonitrile followed by centrifugation under the same condition. After the supernatant was collected, the precipitate was resuspended with 400 μL of acetonitrile followed by centrifugation under the same condition. This procedure was repeated twice, ultimately resulting in an extraction efficacy of 94%. The combined supernatants were centrifuged 7,000×*g* for 3 min at 4 °C. After the precipitate was removed, the supernatant was combined with 1 mL of 25 mM ammonium formate aqueous solution and analyzed using HPLC (Column: YMC-Pack ODS-A, 5 μm, 10×250 mm; Eluent: acetonitrile/25 mM ammonium formate = 36/64; Flow rate: 3.0 mL/min; UV: 254 nm). Fractions were collected at 24-s intervals, and their radioactivity was measured using a gamma counter (1282 CompuGamma CS).

2.8. Analysis of effect of P-glycoprotein (P-gp) inhibition of [^{18}F]3 brain uptake in mice

A PET study in mice was performed using a small animal PET scanner (MIP-100, Sumitomo

This article is protected by copyright. All rights reserved.

Heavy Industries).[44] Eight week-old ddY mice (male, 35.4 ± 0.9 g; Japan SLC; n = 4 for each group) received intravenous injection of 25 mg/kg of cyclosporine A (CsA) (4 mg/mL in physiologic saline; Novartis, Basel, Switzerland). Control mice were treated with 6.3 mL/kg of physiologic saline. Thirty minutes after the pre-treatment, the mice were given 17.7 ± 1.6 MBq of [^{18}F]**3** via the tail vein under anesthesia with 1.5 % (*v*/*v*) isoflurane, and a 60-min dynamic scan was performed immediately after the injection. The resulting sinograms were reconstructed into 21 frames (8 × 30 s, 3 × 60 s, 2 × 120 s, 2 × 180 s, 3 × 300 s, 2 × 540 s, 1 × 600 s) using an interactive reconstruction algorithm (3-dimensional ordered-subset expectation maximization, provided by Sumitomo Heavy Industries; 1 iteration, 32 subsets). The final data sets consisted of 31 slices, with a slice thickness of 0.85 mm and an in-plane image matrix of 256 × 256 pixels (0.3 × 0.3 mm pixel size). The data sets were fully corrected for random coincidences and scatter. Standardized uptake value images were obtained by normalizing tissue radioactivity concentrations according to the injected dose and body weight using PMOD software (PMOD Technologies, Zurich, Switzerland). Regions of interest were drawn over the whole brain to calculate brain uptake and generate time-activity curves.

2.9. Statistical analysis

The biodistribution and organ/blood ratios of radioligands in normal mice were statistically analyzed by multiple *t*-tests corrected by the Holm-Šídák method using GraphPad Prism

This article is protected by copyright. All rights reserved.

Software.

3. RESULTS AND DISCUSSION

3.1. Chemistry

The synthetic route for reference compound **3** and chlorinated ^{18}F-labeling precursor **8** are shown in Scheme 1. To introduce a fluoroethyl moiety, 2-fluoroethyl p-toluenesulfonate (**4**) was prepared by monofluorination of ethylene di(*p*-toluenesulfonate) with tetrabutylammonium fluoride (TBAF). Compound **5** was synthesized according to a published method from 1,2,3,4-tetrahydro-9*H*-pyrido[3,4-*b*]indole.[42] For synthesis of **3**, **5** was *N*-fluoroethylated with **4**, and then a methylester group was converted to a hydroxamic acid group with hydroxylamine. For synthesis of **8**, **5** was *N*-hydroxyethylated with 2-bromoethanol and then chlorinated with thionyl chloride. Initially, we attempted to synthesize a tosylated precursor from **5** with ethylene di(*p*-toluenesulfonate) under the same reaction condition used for the synthesis of **6**, but formation of a dimerized by-product, which was bridged with an ethylene group, was mainly observed. We also tried tosylation of **7** using tosyl chloride with triethylamine or *N*,*N*,*N*',*N*'-tetramethyl-1,3-propanediamine as a base,[45] but we failed to obtain the desired product. A fluorination test of **8** using TBAF in acetonitrile under heating demonstrated formation of **6** (data not shown), therefore we proceeded to radiosynthesis of [^{18}F]**3** using **8** as a precursor.

This article is protected by copyright. All rights reserved.

3.2. Radiosynthesis of [^{18}F]3

Radiosynthesis of [^{18}F]**3** was achieved with a two-step reaction (Scheme 2). The radiochemical yield after HPLC purification of [^{18}F]**3** was 13 ± 4% (n = 3). The radiochemical purity and molar activity of the [^{18}F]**3** saline solution at the end of synthesis were 97.2 ± 0.3% and 185 ± 56 GBq/μmol, respectively. The total synthesis time was 80–90 min from the end of bombardment.

3.3. Lipophilicity determination

We determined the lipophilicity of [^{18}F]**3** using the shake-flask method, and the log *D* value was 2.0, which is within the range of preferable lipophilicity for crossing the BBB.[46]

3.4. HDAC6 selectivity

Binding selectivity of compounds **2** and **3** was evaluated by inhibition assays against HDAC1, as a representative HDAC, and HDAC6 (Figure 2 and Table 1). As shown in Figure 2, inhibition curves for HDAC1 and HDAC6 of the fluoroethyl analogue **3** were almost identical to those of **2**, with an IC_{50} value of 33.1 nM toward HDAC6 and a selectivity of approximately 30-fold over HDAC1. These results were consistent with our expectation, which was that introducing a fluoroethyl group to the nitrogen atom of the β-carboline structure would have a

This article is protected by copyright. All rights reserved.

negligible effect on HDAC6 selectivity. Notably, the concentration of HDAC1 in the human brain is 10-fold greater than that of HDAC6,[34] therefore, the selectivity of [^{18}F]**3** is an important factor for HDAC6 imaging. Compared with our result, however, a previous study reported a higher binding affinity of compound **2** for HDAC6, with an IC_{50} value of 1.40 nM and a 3700 fold selectivity over HDAC1.[42] This discrepancy may have been caused by differences in enzyme activity assay systems. Additionally, it was reported that one of the two catalytic domains of HDAC6 deacetylated a broad variety of substrates, whereas the other catalytic domain has a high specificity for substrates with C-terminal acetyllysine residues.[13] Therefore, inhibition assays for HDAC6 activity using fluorogenic substrates specific for one catalytic domain may overlook interactions between the inhibitors and the other catalytic domain. To determine the accurate binding affinities of ligands for the HDACs and dispel the above concerns in the future, the development of direct binding assay system, such as a saturation binding assay using radiolabeled ligands, is required.

3.5. Biodistribution in normal mice

The biodistribution of [^{11}C]**2** and [^{18}F]**3** from 1 min to 60 min post-injection was evaluated in normal mice (Table 2). Excellent stability of [^{11}C]**2** was demonstrated in plasma radio-metabolite analysis in mice;[39] therefore, the comparison of pharmacokinetics between the radioligands could reveal the influence of structural modifications, such as the introduction of

This article is protected by copyright. All rights reserved.

an [^{18}F]fluoroethyl moiety, of [^{18}F]**3** on its pharmacokinetics. The initial blood radioactivity of [^{18}F]**3** was higher than that of [^{11}C]**2** (4.3% ID/g versus 2.3% ID/g at 2 min post-injection), although both radioactivity levels gradually decreased over time and reached the same degree at 60 min post-injection. Similarly, in some organs the radioactivity uptake of [^{18}F]**3**-injected mice was significantly higher than observed with [^{11}C]**2**-injected mice, including the heart, lung, liver, and muscle, at the early time points. High radioactivity was observed in the liver, kidney, and small intestine, suggesting that the radioligands were excreted by both renal and hepatobiliary excretion. Brain uptake of [^{11}C]**2** was less than 0.5% ID/g over a 60-min period, and this observed poor BBB permeability is consistent with previous reports.[38,39] Similarly, brain uptake of [^{18}F]**3** was low and stable at around 0.5% ID/g over a 60-min period. Murine testis is a known to exhibit high expression levels of HDAC6.[47] The development and function of the testis of HDAC6-knockout mice are normal,[48] whereas inhibition of HDAC6 restricts sperm motility in rats through increased levels of acetyl α-tubulin, which is a component of microtubules in the flagella.[49] In our study, however, testis radioactivity was below blood levels at every time point for both [^{11}C]**2** and [^{18}F]**3**. As with the brain, the testis has a blood-testis barrier to protect spermatocytogenesis from toxicants in the systemic circulation and autoimmune responses;[50] therefore, the barrier may inhibit testis uptake of the radioligands. Although radioactivity uptake in the brain and testis of [^{18}F]**3**-injected mice was higher than in [^{11}C]**2**-injected mice at several time points, the brain-to-blood and testis-to-blood uptake ratios

This article is protected by copyright. All rights reserved.

of the radioligands were almost identical. Bone radioactivity of [^{18}F]**3**-injected mice peaked at 2.6% ID/g at 10 min post-injection followed by a slight decrease over time. The [^{18}F]fluoride ion is characterized by accumulation in the bone, therefore it appears that [^{18}F]**3** has a high tolerance to in vivo defluorination.

The deacetylation and ubiquitin-binding functions of HDAC6 play important roles in cancer growth, cell survival, and metastasis through many signaling pathways,[22] therefore, noninvasive imaging of HDAC6 will aid diagnosis or development of HDAC6-targeting drugs for cancers. However, because [^{18}F]**3** demonstrated high radioactivity uptake in the organs of the abdomen and chest, the application of this radioligand will be limited to cancers localized in other areas. For example, increased expression of HDAC6 is observed in several cancers, including oral squamous cell carcinoma and malignant melanoma.[51,52] The expression of HDAC6 is regulated by estradiol in estrogen receptor α positive breast cancer cells and may serve as a prognostic indicator.[17,53] Furthermore, HDAC6 selective inhibitors have been evaluated in pre-clinical and clinical trials against cancers such as glioblastoma, multiple myeloma, and malignant melanoma.[23,54] At the late time points in the biodistribution assay, the radioactivity levels of blood and muscle of [^{18}F]**3**-injected mice were comparable to those of [^{11}C]**2**-injected mice, which demonstrated specific uptake to B16F10 melanoma cells grafted in mice with a tumor/muscle ratio of approximately 3 in a small animal PET study.[39] Therefore, use of [^{18}F]**3** for PET imaging of these cancers is justified.

This article is protected by copyright. All rights reserved.

3.6. Metabolite analysis

The metabolic stability of [^{18}F]**3** in mouse plasma was determined by HPLC analysis (Figure 3 and Table 3). The percentages of the intact radioligand gradually decreased with time and were 76 ± 3% and 70 ± 12% at 15 and 30 min post-injection, respectively. In addition to unchanged [^{18}F]**3**, two polar radioactive metabolites were observed in mouse plasma. In comparison, analysis of the metabolism of the Tubastatin A analogue [^{11}C]KB631 indicated that the percentage of the unchanged form in mouse plasma were 98 and 84% after 10 and 60 min post-injection, respectively.[39] The in vivo stability of [^{11}C]Martinostat in rodents and non-human primates has been reported. The degradation of [^{11}C]Martinostat is limited at 30 min post-injection in rat brains,[33] whereas the proportion of unchanged [^{11}C]Martinostat remained around 40 % in plasma 30 min post-injection in baboons.[33,55] A study using carbon-11 labeled MS-275, a benzamide HDAC inhibitor undergoing clinical trials for cancer treatment, reported that the percentage of the unchanged form in baboon plasma was approximately 60% 40 min post-injection.[56] Compared with these radioligands, the metabolic stability and tolerance to defluorination in mice of [^{18}F]**3** are considered to be acceptable for in vivo imaging, but further studies to characterize the chemical species of radiometabolites and to determine the stability in non-human primates are needed.

This article is protected by copyright. All rights reserved.

3.7. Effect of P-gp inhibition on brain uptake of [^{18}F]3

We assessed the influence of P-gp, a multidrug-resistance-associated protein, on the brain kinetics of [^{18}F]**3**. Small animal PET studies were performed in mice with or without pre-treatment with the P-gp inhibitor CsA, and the brain time-activity curves were compared (Figure 4a and 4b). P-gp inhibition had no effect on the brain uptake of [^{18}F]**3** until 10 min after injection. On the other hand, time-activity curves showed that the brain radioactivity of mice with P-gp inhibition was slightly higher than that of control mice during the late scan period. In summed PET images of the mouse heads at 30 min post-injection (Figure 4c), an increase in back-ground radioactivity was confirmed in the mice with P-gp inhibition compared with the control mice. This increased radioactivity appeared to spill over into the brain region of interest, resulting in the observed difference in the time-activity curves. It is known that CsA is a substrate of cytochrome P450 3A4;[57,58] therefore, inhibition of this enzyme by CsA treatment may have reduced the metabolism and excretion of [^{18}F]**3** in mice.

Generally, characteristics such as low molecular weight (<500 Da) and moderate lipophilicity (2.0–3.5 in log *D*) indicate, but do not guarantee, that compounds will exhibit good BBB permeability.[46] The molecular weight and log *D* value of **3** are 367 Da and 2.0, respectively; however, its brain uptake in mice is quite low. This discrepancy may be attributed to, as Kozikowski et al. suggested, the effect of pK_a values of certain HDAC inhibitors with a hydroxamic acid moiety on BBB permeability.[59] These authors used in vitro membrane

This article is protected by copyright. All rights reserved.

permeability studies to demonstrate that compounds containing a basic cap group with a high pK_a value (more than approximately 5.9) tended to have low membrane permeability, which was likely due to ionization at physiological pH. The pK_a value of the basic cap group of Tubastatin A is relatively high (7.14);[59] therefore, lowering the pK_a values by structural modification may improve the BBB permeability of Tubastatin A analogues.

Accepted Article

This article is protected by copyright. All rights reserved.

4. CONCLUSIONS

In summary, we report the radiosynthesis and biological evaluation of a novel ^{18}F-labeled Tubastatin A analogue [^{18}F]**3** for PET imaging of HDAC6. The radiosynthesis of [^{18}F]**3** was achieved by a two-step reaction composed of ^{18}F-fluorination and hydroxamic acid formation, which was readily applied to an automatic radiosynthesizer. The HDAC6 selectivity of **3** was almost identical to that of a methylated analogue KB631. Biodistribution studies in mice revealed the poor BBB permeability of [^{18}F]**3**, suggesting a limitation for studies into neurodegenerative diseases. Meanwhile, the characteristics of [^{18}F]**3**, such as steady clearance from blood and muscle, moderate metabolic stability, and high tolerance to in vivo defluorination, encourage further evaluation of its utility for imaging of certain cancers.

Accepted Article

This article is protected by copyright. All rights reserved.

ACKNOWLEDGEMENTS

We thank Mr. Kunpei Hayashi, Mr. Masanari Sakai, and Mr. Kosuke Nishino (SHI Accelerator Service Ltd., Tokyo, Japan) for technical assistance with the cyclotron operation and radiosynthesis. This work was supported by a Grant-in-Aid for Research Activity Start-up No. 16H07486 and a Grant-in-Aid for Young Scientists No. 18K15655 from the Japan Society for the Promotion of Science and an internal grant from Tokyo Metropolitan Institute of Gerontology.

CONFLICT OF INTEREST

Jun Toyohara received a research grant from Sumitomo Heavy Industries (Tokyo, Japan).

Accepted Article

This article is protected by copyright. All rights reserved.

Accepted Article

REFERENCES

1. Strahl BD, Allis CD. The language of covalent histone modifications. *Nature.* 2000;403(6765):41-45.

2. de Ruijter AJ, van Gennip AH, Caron HN, Kemp S, van Kuilenburg AB. Histone deacetylases (HDACs): characterization of the classical HDAC family. *Biochem J.* 2003;370(Pt 3):737-749.

3. Wagner FF, Wesmall yi UM, Lewis MC, Holson EB. Small molecule inhibitors of zinc-dependent histone deacetylases. *Neurotherapeutics.* 2013;10(4):589-604.

4. Barneda-Zahonero B, Parra M. Histone deacetylases and cancer. *Mol Oncol.* 2012;6(6):579-589.

5. Yao YL, Yang WM. Beyond histone and deacetylase: an overview of cytoplasmic histone deacetylases and their nonhistone substrates. *J Biomed Biotechnol.* 2011;2011:146493.

6. Barrett RM, Wood MA. Beyond transcription factors: the role of chromatin modifying enzymes in regulating transcription required for memory. *Learn Mem.* 2008;15(7):460-467.

7. Giannini G, Cabri W, Fattorusso C, Rodriquez M. Histone deacetylase inhibitors in the treatment of cancer: overview and perspectives. *Future Med Chem.* 2012;4(11):1439-1460.

This article is protected by copyright. All rights reserved.

8. Mottamal M, Zheng S, Huang TL, Wang G. Histone deacetylase inhibitors in clinical studies as templates for new anticancer agents. *Molecules.* 2015;20(3):3898-3941.

9. Didonna A, Opal P. The promise and perils of HDAC inhibitors in neurodegeneration. *Ann Clin Transl Neurol.* 2015;2(1):79-101.

10. D'Mello SR. Histone deacetylases as targets for the treatment of human neurodegenerative diseases. *Drug News Perspect.* 2009;22(9):513-524.

11. Batchu SN, Brijmohan AS, Advani A. The therapeutic hope for HDAC6 inhibitors in malignancy and chronic disease. *Clin Sci (Lond).* 2016;130(12):987-1003.

12. Verdel A, Curtet S, Brocard MP, et al. Active maintenance of mHDA2/mHDAC6 histone-deacetylase in the cytoplasm. *Curr Biol.* 2000;10(12):747-749.

13. Hai Y, Christianson DW. Histone deacetylase 6 structure and molecular basis of catalysis and inhibition. *Nat Chem Biol.* 2016;12(9):741-747.

14. Van Helleputte L, Benoy V, Van Den Bosch L. The role of histone deacetylase 6 (HDAC6) in neurodegeneration. *Res Rep Biol.* 2014;5:1-13.

15. Li Y, Shin D, Kwon SH. Histone deacetylase 6 plays a role as a distinct regulator of diverse cellular processes. *FEBS J.* 2013;280(3):775-793.

16. Hubbert C, Guardiola A, Shao R, et al. HDAC6 is a microtubule-associated deacetylase. *Nature.* 2002;417(6887):455-458.

17. Saji S, Kawakami M, Hayashi S, et al. Significance of HDAC6 regulation via estrogen

This article is protected by copyright. All rights reserved.

Accepted Article

signaling for cell motility and prognosis in estrogen receptor-positive breast cancer. *Oncogene.* 2005;24(28):4531-4539.

18. Kawaguchi Y, Kovacs JJ, McLaurin A, Vance JM, Ito A, Yao TP. The deacetylase HDAC6 regulates aggresome formation and cell viability in response to misfolded protein stress. *Cell.* 2003;115(6):727-738.

19. Richter-Landsberg C. Protein aggregate formation in oligodendrocytes: tau and the cytoskeleton at the intersection of neuroprotection and neurodegeneration. *Biol Chem.* 2016;397(3):185-194.

20. Ouyang H, Ali YO, Ravichandran M, et al. Protein aggregates are recruited to aggresome by histone deacetylase 6 via unanchored ubiquitin C termini. *J Biol Chem.* 2012;287(4):2317-2327.

21. Rodriguez-Gonzalez A, Lin T, Ikeda AK, Simms-Waldrip T, Fu C, Sakamoto KM. Role of the aggresome pathway in cancer: targeting histone deacetylase 6-dependent protein degradation. *Cancer Res.* 2008;68(8):2557-2560.

22. Aldana-Masangkay GI, Sakamoto KM. The role of HDAC6 in cancer. *J Biomed Biotechnol.* 2011;2011:875824.

23. Li T, Zhang C, Hassan S, et al. Histone deacetylase 6 in cancer. *J Hematol Oncol.* 2018;11(1):111.

24. Tago T, Toyohara J. Advances in the Development of PET Ligands Targeting Histone

This article is protected by copyright. All rights reserved.

Accepted Article

Deacetylases for the Assessment of Neurodegenerative Diseases. *Molecules.* 2018;23(2).

25. Wang C, Schroeder FA, Hooker JM. Visualizing epigenetics: current advances and advantages in HDAC PET imaging techniques. *Neuroscience.* 2014;264:186-197.

26. Couto PJ, Millis RM. PET Imaging of Epigenetic Influences on Alzheimer's Disease. *Int J Alzheimers Dis.* 2015;2015:575078.

27. Laws MT, Bonomi RE, Kamal S, et al. Molecular imaging HDACs class IIa expression-activity and pharmacologic inhibition in intracerebral glioma models in rats using PET/CT/(MRI) with [^{18}F]TFAHA. *Sci Rep.* 2019;9(1):3595.

28. Schroeder FA, Wang C, Van de Bittner GC, et al. PET imaging demonstrates histone deacetylase target engagement and clarifies brain penetrance of known and novel small molecule inhibitors in rat. *ACS Chem Neurosci.* 2014;5(10):1055-1062.

29. Mukhopadhyay U, Tong WP, Gelovani JG, Alauddin MM. Radiosynthesis of 6-([^{18}F]fluoroacetamido)-1-hexanoicanilide ([^{18}F]FAHA) for PET imaging of histone deacetylase (HDAC). *J Labelled Comp Radiopharm.* 2006;49(11):997-1006.

30. Wanka L, Iqbal K, Schreiner PR. The lipophilic bullet hits the targets: medicinal chemistry of adamantane derivatives. *Chem Rev.* 2013;113(5):3516-3604.

31. Liu J, Obando D, Liao V, Lifa T, Codd R. The many faces of the adamantyl group in drug design. *Eur J Med Chem.* 2011;46(6):1949-1963.

This article is protected by copyright. All rights reserved.

Accepted Article

32. Strebl MG, Wang C, Schroeder FA, et al. Development of a Fluorinated Class-I HDAC Radiotracer Reveals Key Chemical Determinants of Brain Penetrance. *ACS Chem Neurosci.* 2016;7(5):528-533.

33. Wang C, Schroeder FA, Wey HY, et al. In vivo imaging of histone deacetylases (HDACs) in the central nervous system and major peripheral organs. *J Med Chem.* 2014;57(19):7999-8009.

34. Wey HY, Gilbert TM, Zurcher NR, et al. Insights into neuroepigenetics through human histone deacetylase PET imaging. *Sci Transl Med.* 2016;8(351):351ra106.

35. Gilbert TM, Zurcher NR, Wu CJ, et al. PET neuroimaging reveals histone deacetylase dysregulation in schizophrenia. *J Clin Invest.* 2019;129(1):364-372.

36. Butler KV, Kalin J, Brochier C, Vistoli G, Langley B, Kozikowski AP. Rational design and simple chemistry yield a superior, neuroprotective HDAC6 inhibitor, tubastatin A. *J Am Chem Soc.* 2010;132(31):10842-10846.

37. Lu S, Zhang Y, Kalin JH, Cai L, Kozikowski AP, Pike VW. Exploration of the labeling of [^{11}C]tubastatin A at the hydroxamic acid site with [^{11}C]carbon monoxide. *J Labelled Comp Radiopharm.* 2016;59(1):9-13.

38. Lu S, Zhang L, Kalin J, et al. Synthesis and evaluation of [methyl-^{11}C]KB631–a candidate radioligand for histone deacetylase isozyme 6 (HDAC6). *J Labelled Comp Radiopharm.* 2013;56:S319.

This article is protected by copyright. All rights reserved.

39. Vermeulen K, Ahamed M, Luyten K, Bormans G. Evaluation of [^{11}C]KB631 as a PET tracer for in vivo visualisation of HDAC6 in B16·F10 melanoma. *Nucl Med Biol.* 2019;in press.

40. Strebl MG, Campbell AJ, Zhao WN, et al. HDAC6 Brain Mapping with [^{18}F]Bavarostat Enabled by a Ru-Mediated Deoxyfluorination. *ACS Cent Sci.* 2017;3(9):1006-1014.

41. Beyzavi MH, Mandal D, Strebl MG, et al. ^{18}F-Deoxyfluorination of Phenols via Ru pi-Complexes. *ACS Cent Sci.* 2017;3(9):944-948.

42. Kalin JH, Butler KV, Akimova T, Hancock WW, Kozikowski AP. Second-generation histone deacetylase 6 inhibitors enhance the immunosuppressive effects of Foxp3+ T-regulatory cells. *J Med Chem.* 2012;55(2):639-651.

43. Hendricks JA, Keliher EJ, Marinelli B, Reiner T, Weissleder R, Mazitschek R. In vivo PET imaging of histone deacetylases by ^{18}F-suberoylanilide hydroxamic acid (^{18}F-SAHA). *J Med Chem.* 2011;54(15):5576-5582.

44. Ishii K, Kikuchi Y, Matsuyama S, et al. First achievement of less than 1 mm FWHM resolution in practical semiconductor animal PET scanner. *Nucl Instrum Meth A.* 2007;576:435-440.

45. Yoshida Y, Shimonishi K, Sakakura Y, Okada S, Aso N, Tanabe Y. Facile and Practical Methods for the Sulfonylation of Alcohols Using Ts(Ms)Cl and $Me_2N(CH_2)nNMe_2$ as a Key Base. *Synthesis.* 1999;1999(09):1633-1636.

This article is protected by copyright. All rights reserved.

46. Pike VW. PET radiotracers: crossing the blood-brain barrier and surviving metabolism. *Trends Pharmacol Sci.* 2009;30(8):431-440.

47. Seigneurin-Berny D, Verdel A, Curtet S, et al. Identification of components of the murine histone deacetylase 6 complex: link between acetylation and ubiquitination signaling pathways. *Mol Cell Biol.* 2001;21(23):8035-8044.

48. Zhang Y, Kwon S, Yamaguchi T, et al. Mice lacking histone deacetylase 6 have hyperacetylated tubulin but are viable and develop normally. *Mol Cell Biol.* 2008;28(5):1688-1701.

49. Parab S, Shetty O, Gaonkar R, Balasinor N, Khole V, Parte P. HDAC6 deacetylates alpha tubulin in sperm and modulates sperm motility in Holtzman rat. *Cell Tissue Res.* 2015;359(2):665-678.

50. Mruk DD, Cheng CY. The Mammalian Blood-Testis Barrier: Its Biology and Regulation. *Endocr Rev.* 2015;36(5):564-591.

51. Liu J, Gu J, Feng Z, et al. Both HDAC5 and HDAC6 are required for the proliferation and metastasis of melanoma cells. *J Transl Med.* 2016;14(1).

52. Sakuma T, Uzawa K, Onda T, et al. Aberrant expression of histone deacetylase 6 in oral squamous cell carcinoma. *Int J Oncol.* 2006.

53. Zhang Z, Yamashita H, Toyama T, et al. HDAC6 expression is correlated with better survival in breast cancer. *Clin Cancer Res.* 2004;10(20):6962-6968.

This article is protected by copyright. All rights reserved.

Accepted Article

54. Zhang I, Beus M, Stochaj U, et al. Inhibition of glioblastoma cell proliferation, invasion, and mechanism of action of a novel hydroxamic acid hybrid molecule. *Cell Death Discov.* 2018;4(1).

55. Wey HY, Wang C, Schroeder FA, Logan J, Price JC, Hooker JM. Kinetic Analysis and Quantification of [^{11}C]Martinostat for in Vivo HDAC Imaging of the Brain. *ACS Chem Neurosci.* 2015;6(5):708-715.

56. Hooker JM, Kim SW, Alexoff D, et al. Histone deacetylase inhibitor, MS-275, exhibits poor brain penetration: PK studies of [^{11}C]MS-275 using Positron Emission Tomography. *ACS Chem Neurosci.* 2010;1(1):65-73.

57. Ogu CC, Maxa JL. Drug interactions due to cytochrome P450. *Proc (Bayl Univ Med Cent).* 2000;13(4):421-423.

58. Watkins PB. The role of cytochromes P-450 in cyclosporine metabolism. *J Am Acad Dermatol.* 1990;23(6 Pt 2):1301-1309; discussion 1309-1311.

59. Kozikowski AP, Shen S, Pardo M, et al. Brain Penetrable Histone Deacetylase 6 Inhibitor SW-100 Ameliorates Memory and Learning Impairments in a Mouse Model of Fragile X Syndrome. *ACS Chem Neurosci.* 2019;10(3):1679-1695.

Accepted Article

This article is protected by copyright. All rights reserved.

TABLE 1 IC_{50} values of **2** and **3** against HDAC1 and HDAC6 activities

Compound	HDAC1 IC_{50} (nM)	HDAC6 IC_{50} (nM)
2	904 ± 262	30.4 ± 4.7
3	996 ± 226	33.1 ± 5.1

Accepted Article

This article is protected by copyright. All rights reserved.

TABLE 2 Biodistribution of radioactivity in normal mice after injection of [^{11}C]**2** and [^{18}F]**3**

	Time after injection (min)				
Tissue	1	5	10	30	60
*[^{11}C]**2***					
Blood	2.33 (0.15)	1.60 (0.44)	1.61 (0.49)	1.09 (0.21)	0.77 (0.17)
Brain	0.18 (0.05)	0.16 (0.04)	0.19 (0.04)	0.25 (0.02)	0.27 (0.12)
Heart	6.37 (0.94)	5.14 (0.75)	6.02 (0.59)	2.57 (0.26)	1.09 (0.19)
Lung	11.0 (1.48)	7.77 (1.33)	7.35 (1.29)	5.28 (0.67)	3.22 (0.55)
Liver	10.6 (2.00)	12.4 (2.48)	14.1 (2.78)	9.51 (2.30)	5.39 (1.03)
Spleen	2.91 (1.58)	4.49 (0.55)	4.83 (0.19)	2.58 (0.19)	1.46 (0.27)
Stomach	1.88 (0.28)	1.64 (0.15)	3.00 (0.70)	3.15 (0.44)	3.51 (2.53)
Kidney	24.3 (3.39)	19.5 (0.77)	20.1 (2.62)	12.6 (0.58)	7.47 (0.84)
Intestine	5.74 (0.80)	9.17 (4.30)	16.0 (4.15)	16.2 (5.88)	9.11 (5.57)
Testis	0.26 (0.10)	0.38 (0.16)	0.48 (0.20)	0.47 (0.14)	0.38 (0.08)
Muscle	1.78 (0.17)	1.88 (0.15)	1.60 (0.23)	1.03 (0.03)	0.85 (0.13)
Femur	1.62 (0.17)	1.32 (0.38)	1.65 (0.44)	0.91 (0.12)	0.77 (0.14)
Brain/Blood	0.08 (0.02)	0.10 (0.01)	0.12 (0.03)	0.24 (0.07)	0.37 (0.18)
Testis/Blood	0.11 (0.05)	0.26 (0.14)	0.30 (0.06)	0.44 (0.17)	0.50 (0.06)
*[^{18}F]**3***					
Blood	4.26 (0.32)‡	4.26 (0.39)‡	3.28 (0.24)†	1.72 (0.42)	1.16 (0.30)
Brain	0.36 (0.06)†	0.43 (0.03)‡	0.42 (0.05)‡	0.55 (0.10)†	0.45 (0.08)
Heart	10.6 (1.33)†	7.79 (1.14)*	6.18 (0.73)	2.46 (0.35)	1.58 (0.36)
Lung	16.2 (1.41)†	12.6 (0.68)†	10.1 (2.78)	3.76 (0.33)*	2.29 (0.68)
Liver	20.5 (4.17)*	18.0 (3.18)	18.2 (0.35)	9.75 (0.97)	4.91 (1.04)
Spleen	4.58 (1.51)	6.25 (1.30)	5.27 (1.00)	2.93 (0.13)	1.81 (0.41)
Stomach	2.68 (1.17)	3.33 (0.50)†	4.07 (0.83)	3.71 (1.11)	1.46 (0.25)
Kidney	24.6 (0.85)	19.8 (1.82)	17.9 (1.25)	8.33 (0.64)‡	4.66 (0.89)*
Intestine	9.13 (1.98)	18.9 (5.85)	28.9 (3.23)*	18.8 (6.03)	10.4 (2.04)
Testis	0.27 (0.04)	0.54 (0.09)	0.65 (0.11)	0.83 (0.04)*	0.68 (0.12)*
Muscle	2.74 (0.41)*	3.01 (0.27)†	2.22 (0.17)*	1.33 (0.20)	0.88 (0.13)
Femur	1.77 (0.17)	2.56 (0.36)*	1.82 (0.13)	1.48 (0.14)†	1.26 (0.27)
Brain/Blood	0.08 (0.01)	0.10 (0.01)	0.13 (0.01)	0.33 (0.05)	0.40 (0.08)
Testis/Blood	0.07 (0.01)	0.13 (0.01)	0.20 (0.03)	0.70 (0.46)	0.59 (0.09)

Data are expressed as mean (standard deviation) of % ID/g (n = 4).

$^{*}P \leq 0.05$; $^{\dagger}P \leq 0.01$; $^{\ddagger}P \leq 0.001$ vs [^{11}C]**2**.

This article is protected by copyright. All rights reserved.

TABLE 3 Radioactivity percentages of unchanged [^{18}F]**3** and metabolites in mouse plasma

Time after injection (min)	Radioactivity % to total radioactivity in plasma		
	Metabolite 1 (RT = 4.0 min)	Metabolite 2 (RT = 7.5 min)	[^{18}F]**3** (RT = 9.5 min)
15	12.3 (1.6)	10.1 (1.4)	76.4 (3.0)
30	20.4 (11.0)	8.9 (0.8)	70.0 (12.0)

Data are expressed as mean (standard deviation) (n = 3).

RT: retention time.

Accepted Article

This article is protected by copyright. All rights reserved.

Figure 1

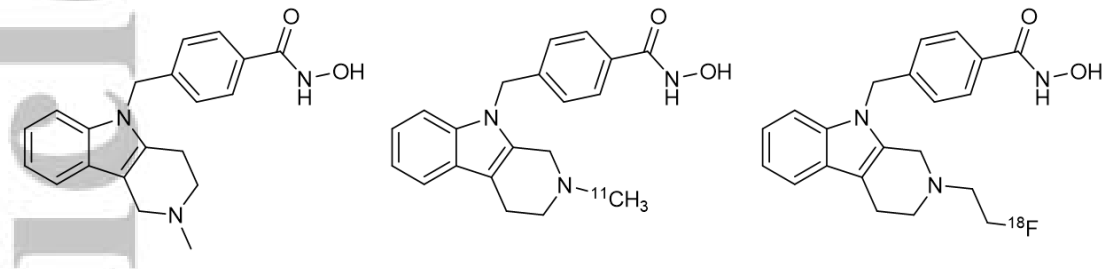

1 (Tubastatin A) [^{11}C]**2** ([^{11}C]KB631) [^{18}F]**3**

FIGURE 1 Chemical structures of Tubastatin A and its radiolabeled analogues

Accepted Article

This article is protected by copyright. All rights reserved.

Accepted Article

Figure 2

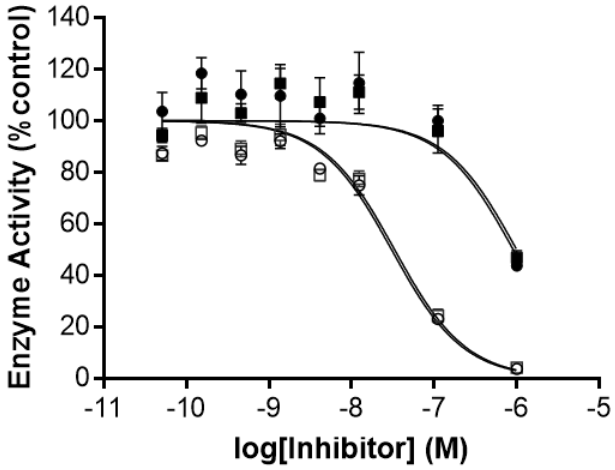

FIGURE 2 Inhibition curves of compounds **2** and **3** against enzyme activities of HDAC1 and HDAC6. filled circle: **2** for HDAC1; filled square: **3** for HDAC1; open circle: **2** for HDAC6; open square: **3** for HDAC6. Data are expressed as mean. Bars represent standard deviation (n = 3)

This article is protected by copyright. All rights reserved.

Accepted Article

Figure 3

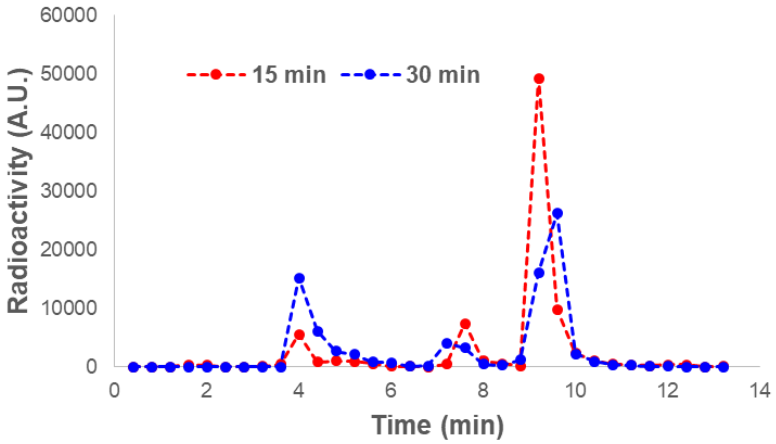

FIGURE 3 Representative chromatograms of radio-HPLC analysis of plasma from mice 15 and 30 min post-injection of [^{18}F]**3** (retention time = 9.5 min)

This article is protected by copyright. All rights reserved.

Accepted Article

Figure 4

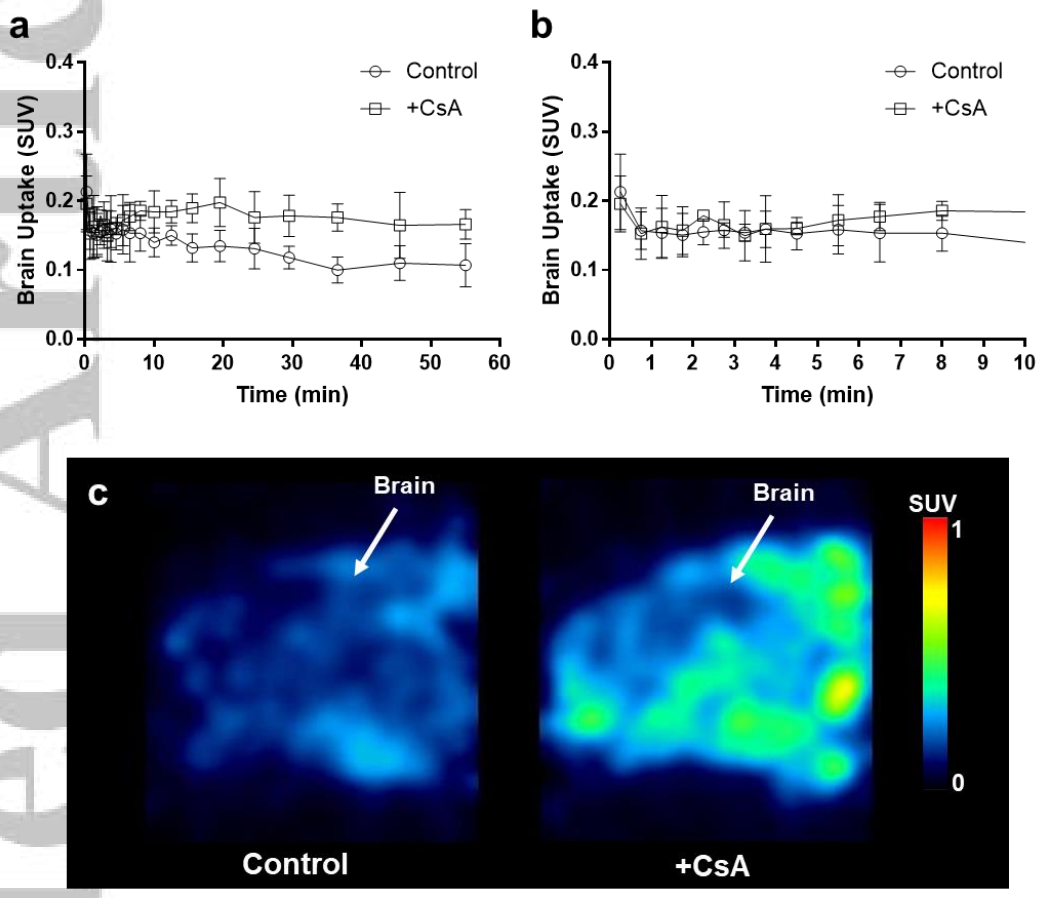

FIGURE 4 PET studies of the effect of P-gp blockade on [^{18}F]**3** brain kinetics. **a** shows brain time-activity curves of [^{18}F]**3** in mice with (circle) and without (square) pre-treatment with cyclosporine A (+CsA). **b** shows data during the early post-injection period in **a**. **c** shows typical [^{18}F]**3** PET images (27–32 min post-injection, sagittal views) of mouse heads with (+CsA, right) or without (Control, left) cyclosporine A pre-treatment. Data are expressed as mean. Bars represent standard deviation (n = 4)

This article is protected by copyright. All rights reserved.

Scheme 1

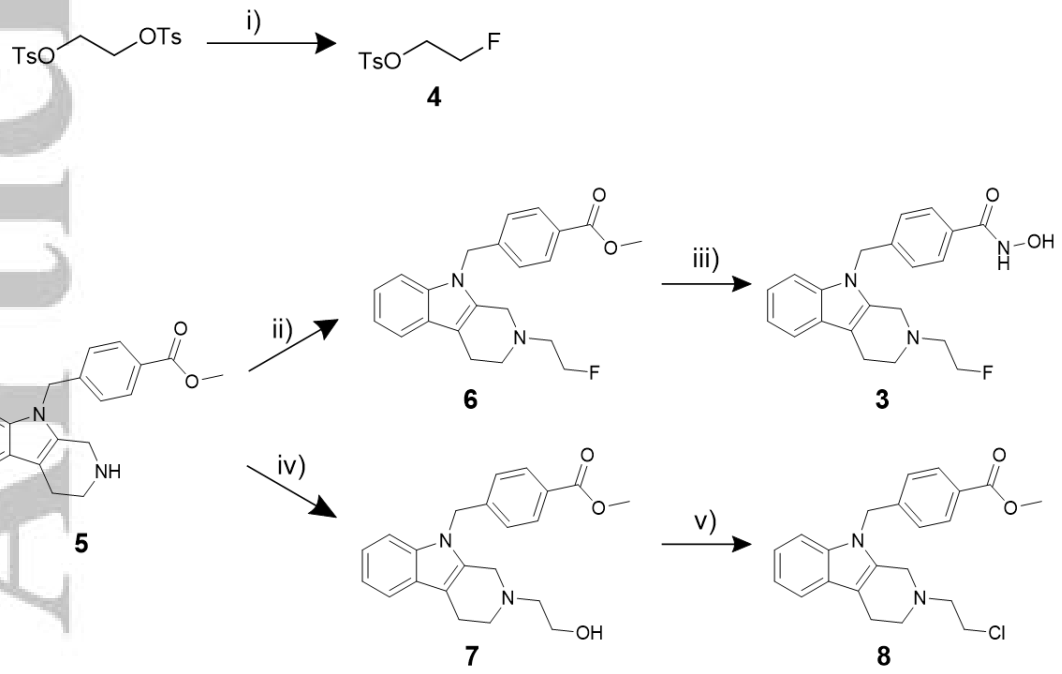

SCHEME 1 Chemical synthesis of compounds **3**–**8**. i) TBAF, acetonitrile, 80 °C, 2 h; ii) **4**, triethylamine, dimethylformamide, 60 °C, 3 h; iii) 50% hydroxylamine in water, saturated sodium hydroxide in methanol, methanol, tetrahydrofuran, 0 °C, 2 h, rt, 3 h; iv) 2-bromoethanol, potassium carbonate, acetonitrile, 80°C, 3.5 h; v) thionyl chloride, dichloromethane, rt, 4.5 h

Accepted Article

This article is protected by copyright. All rights reserved.

Scheme 2

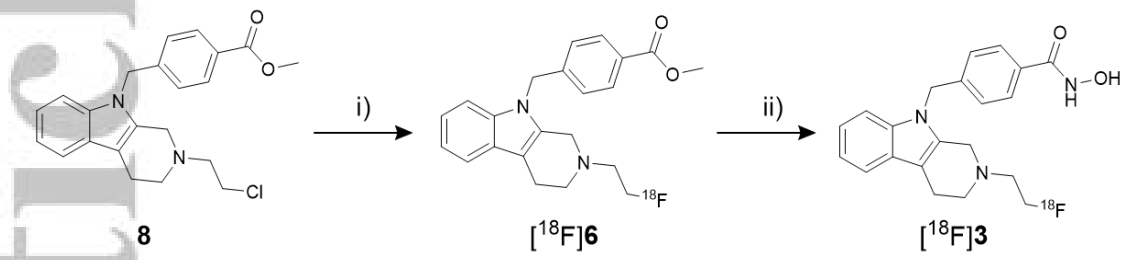

SCHEME 2 Radiosynthesis of [^{18}F]**3** from **8**. i) [^{18}F]TBAF, acetonitrile, 90 °C, 15 min; ii) 50% hydroxylamine in water, 2 M sodium hydroxide in methanol, 30 °C, 10 min

Accepted Article

This article is protected by copyright. All rights reserved.